



Article

# Structural and Optoelectronic Properties of Two-Dimensional Ruddlesden–Popper Hybrid Perovskite CsSnBr<sub>3</sub>

Guangbiao Xiang<sup>1</sup>, Yanwen Wu<sup>1</sup>, Yushuang Li<sup>1</sup>, Chen Cheng<sup>1,\*</sup>, Jiancai Leng<sup>2,\*</sup> and Hong Ma<sup>1,\*</sup>

<sup>1</sup> Shandong Provincial Key Laboratory of Optics, Photonic Device and Collaborative Innovation Center of Light Manipulations and Applications, School of Physics and Electronics, Shandong Normal University, Jinan 250014, China; m17753643157@163.com (G.X.); ywwu\_1209@163.com (Y.W.); lys3573172070@163.com (Y.L.)

<sup>2</sup> School of Electronic and Information Engineering (Department of Physics), Qilu University of Technology (Shandong Academy of Sciences), Jinan 250353, China

\* Correspondence: drccheng@sdnu.edu.cn (C.C.); jiancaileng@qlu.edu.cn (J.L.); mahong@sdnu.edu.cn (H.M.)

**Abstract:** Ultrathin inorganic halogenated perovskites have attracted attention owing to their excellent photoelectric properties. In this work, we designed two types of Ruddlesden–Popper hybrid perovskites, Cs<sub>n+1</sub>Sn<sub>n</sub>Br<sub>3n+1</sub> and Cs<sub>n</sub>Sn<sub>n+1</sub>Br<sub>3n+2</sub>, and studied their band structures and band gaps as a function of the number of layers ( $n = 1–5$ ). The calculation results show that Cs<sub>n+1</sub>Sn<sub>n</sub>Br<sub>3n+1</sub> has a direct bandgap while the bandgap of Cs<sub>n</sub>Sn<sub>n+1</sub>Br<sub>3n+2</sub> can be altered from indirect to direct, induced by the 5p-Sn state. As the layers increased from 1 to 5, the bandgap energies of Cs<sub>n+1</sub>Sn<sub>n</sub>Br<sub>3n+1</sub> and Cs<sub>n</sub>Sn<sub>n+1</sub>Br<sub>3n+2</sub> decreased from 1.209 to 0.797 eV and 1.310 to 1.013 eV, respectively. In addition, the optical absorption of Cs<sub>n+1</sub>Sn<sub>n</sub>Br<sub>3n+1</sub> and Cs<sub>n</sub>Sn<sub>n+1</sub>Br<sub>3n+2</sub> was blue-shifted as the structure changed from bulk to nanolayer. Compared with that of Cs<sub>n+1</sub>Sn<sub>n</sub>Br<sub>3n+1</sub>, the optical absorption of Cs<sub>n</sub>Sn<sub>n+1</sub>Br<sub>3n+2</sub> was sensitive to the layers along the  $z$  direction, which exhibited anisotropy induced by the SnBr<sub>2</sub>-terminated surface.

**Keywords:** 2D Ruddlesden–Popper hybrid perovskites; first-principles study; band structures; optoelectronic properties



**Citation:** Xiang, G.; Wu, Y.; Li, Y.; Cheng, C.; Leng, J.; Ma, H. Structural and Optoelectronic Properties of Two-Dimensional Ruddlesden–Popper Hybrid Perovskite CsSnBr<sub>3</sub>. *Nanomaterials* **2021**, *11*, 2119. <https://doi.org/10.3390/nano11082119>

Academic Editors: Filippo Giannazzo and Byungwoo Park

Received: 25 July 2021

Accepted: 18 August 2021

Published: 20 August 2021

**Publisher's Note:** MDPI stays neutral with regard to jurisdictional claims in published maps and institutional affiliations.



**Copyright:** © 2021 by the authors. Licensee MDPI, Basel, Switzerland. This article is an open access article distributed under the terms and conditions of the Creative Commons Attribution (CC BY) license (<https://creativecommons.org/licenses/by/4.0/>).

## 1. Introduction

Perovskites have become competitive candidate materials for photovoltaic and optoelectronic applications, such as solar cells, optically pumped lasers, detectors and light emitting diodes [1–5]. At present, the power-conversion efficiency of perovskite solar cells has reached 25.4% [6]. Over the past several years, the high-performance perovskite light-emitting diodes have developed rapidly, reaching high external quantum efficiencies of over 20% [1]. At room temperature, the optically pumped laser made from the lead halide perovskite nanowires can be tuned in the whole visible spectrum region (420–710 nm) with high-quality factors and low lasing thresholds [3]. The advantages of these materials include their long carrier lifetimes and diffusion lengths, large absorption coefficients in the visible spectrum, small effective masses, tunable bandgaps and high quantum efficiency [7–12]. In addition, compared with other materials, perovskites have the advantage of low-cost and facile processing [13,14]. Although many achievements in the application of lead-based perovskites have been obtained, there are still many challenges, especially due to the presence of toxic lead. The toxicity of lead can cause serious damage to life and the environment. Therefore, the use of less toxic materials, such as tin and other alkaline earth metals, to replace lead has been widely investigated [15]. An inorganic substitute can reduce hysteresis loss that is caused by the presence of methylammonium. Previous work showed that CsPbBr<sub>3</sub> solar cells are as efficient as and have higher levels of environmental stability than CH<sub>3</sub>NH<sub>3</sub>PbBr<sub>3</sub> solar cells, even after aging for 2 weeks [16].

Recently, two-dimensional (2D) Ruddlesden–Popper (RP) hybrid perovskite materials have attracted intensive attention because of their wide applications [17–23]. Compared

with bulk perovskites, 2D perovskites show many unique properties. For example, 2D RP perovskites have a narrow full width at half maximum and blue-shift photoluminescence signal with the decrease in the number of layers owing to the quantum confinement of carriers [24]. Two-dimensional RP perovskites have a higher chemical stability because of the linking of organic molecules, such as  $\text{CH}_3(\text{CH}_2)_3\text{NH}_3$  and  $\text{CH}_3\text{NH}_3$ , on the terminated surface [25]. Ultrathin 2D RP perovskite solar cells can also reduce production costs from the point of view of mass production [26,27]. Until recently, the layer numbers and the size of synthesized ultrathin 2D RP films have been accurately controlled experimentally. Importantly, the bandgap of 2D RP perovskites can be easily adjusted by changing the number of layers [28]. Therefore, the layer-dependent properties of perovskites further enrich their applications in optoelectronic and photovoltaic fields [28–30]. In addition, it is generally known that different terminated surfaces of 2D RP perovskites are important for optoelectronic properties and applications, such as chemical activity of the surfaces, sensing effects, and ultrathin film production. Previous work has reported that the iodine defect improves the efficiency of photoabsorbance in a  $\text{SnBr}_2$ -terminated surface perovskite solar cell by lowering its energy gap [31]. Ab initio calculations of the structural and electronic properties of the CsBr- and  $\text{CaBr}_2/\text{GeBr}_2/\text{SnBr}_2$ -terminated (001) surfaces of  $\text{CsMBr}_3$  ( $M = \text{Ca}, \text{Ge}, \text{Sn}$ ) perovskites indicated noticeable changes of the surface properties in comparison with those for bulk materials [32]. Thus far, there have been many literatures about 2D perovskites with different surface terminations, including the structural and electronic properties, surface relaxations, energetics, bonding properties, ferroelectrics and dipole moment [33–40]. The  $\text{SrTiO}_3$  (100) surface relaxation and rumpling have been calculated with two different terminations ( $\text{SrO}$  and  $\text{TiO}_2$ ) [39]. Experimentally, the researchers have already studied the ferroelectric relaxation, surface relaxation, polar oxide and surface rumpling of perovskites with different surface terminations [41–46]. Particularly, A. Ikeda et al. determined surface rumpling and relaxation of  $\text{TiO}_2$ -terminated  $\text{SrTiO}_3$  (001) using the medium energy ion scattering, and found that the occupation fraction of the  $\text{TiO}_2$  face ranged from 85 to 95% [45].

Herein, we have designed two models based on  $\text{CsSnBr}_3$  with different surface terminations:  $\text{Cs}_{n+1}\text{Sn}_n\text{Br}_{3n+1}$  and  $\text{Cs}_n\text{Sn}_{n+1}\text{Br}_{3n+2}$ . The terminated surfaces are CsBr and  $\text{SnBr}_2$  for the two models, respectively. We investigated the structural and optoelectronic properties, including band structures, surface relaxation effects, density of states and optical absorption spectra of the two models using the first-principles method.  $\text{Cs}_{n+1}\text{Sn}_n\text{Br}_{3n+1}$  and  $\text{Cs}_n\text{Sn}_{n+1}\text{Br}_{3n+2}$  with different numbers of layers showed different properties in the bandgap and absorption coefficient. The theoretical calculation results obtained in the present work can serve as a guideline in the design of different structures and for the improvement of the efficiency of optical absorbance for 2D inorganic perovskites.

## 2. Computational Model and Method

The first-principles calculation in this work is based on density functional theory (DFT) [47]. The calculation method was the all-electron-like projector augmented wave method and the exchange correlation potential realized by Perdew–Burke–Erserch (PBE) in the Vienna Ab Initio Simulation Package (VASP) [48–50]. The electron exchange correction function was described by the generalized gradient approximation parameterized by PBE. The cut-off energy of the plane wave was set to 500 eV. All atoms were allowed to relax until the Hellmann–Feynman forces reached the convergence criterion of less than 0.01 eV/Å. The convergence threshold of energy was set at  $10^{-5}$  eV. The Monkhorst-Pack scheme was used to sample  $k$ -points in the Brillouin zone [51]. The  $k$ -point meshes were set to  $6 \times 6 \times 1$  and  $8 \times 8 \times 1$  for the electronic structure and density of states, respectively. The HSE06 hybrid functional used to calculate the bandgap and the fraction of exact exchange in the Hartree–Fock/DFT hybrid functional-type calculation was 25%. The spin–orbital coupling (SOC) interaction of the Sn atom is weaker than that of heavy atom lead, so the SOC interaction is ignored in our calculation.

As mentioned earlier, a differently terminated surface will change the band structure, optical absorption and bandgap energy of perovskites. In order to further explore the layer dependence of different surface terminations, we designed two models, namely,  $\text{Cs}_{n+1}\text{Sn}_n\text{Br}_{3n+1}$  and  $\text{Cs}_n\text{Sn}_{n+1}\text{Br}_{3n+2}$  ( $n = 1-5$ ), as Type 1 and Type 2 based on the cubic phase structure (Pm3m space group) of three-dimensional  $\text{CsSnBr}_3$  [52], shown in Figure 1. A two-layer Type 2 molecule ( $\text{Cs}_2\text{Sn}_3\text{Br}_8$ ) was structured by a one-layer Type 1 molecule ( $\text{Cs}_2\text{Sn}_1\text{Br}_4$ ), which added one plane composed by one Sn atom and four Br atoms on both the top and bottom surfaces, respectively. The same rule can be applied to multiple-layer structures, namely  $\text{Cs}_n\text{Sn}_{n+1}\text{Br}_{3n+2}$  ( $n = j + 1$ ), which contain  $\text{Cs}_{n+1}\text{Sn}_n\text{Br}_{3n+1}$  ( $n = j$ ). A vacuum region of 10 Å in the  $z$  direction was set on the bottom and top of the models to avoid interaction between the atoms. The electronic configurations of the chemical elements of  $\text{Cs}_{n+1}\text{Sn}_n\text{Br}_{3n+1}$  and  $\text{Cs}_n\text{Sn}_{n+1}\text{Br}_{3n+2}$  included  $4s^24p^5$  (Br),  $5s^25p^66s^1$  (Cs) and  $5s^25p^2$  (Sn) [32].

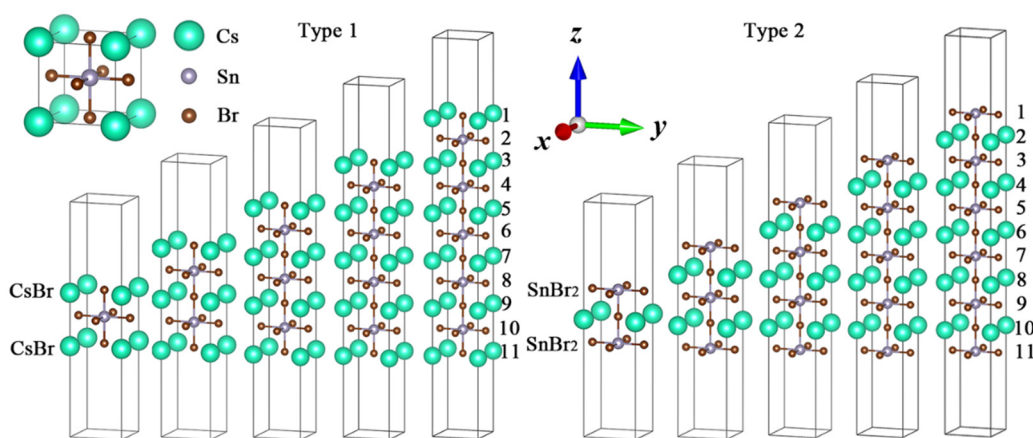


**Figure 1.** Surface models of ultrathin  $\text{CsSnBr}_3$  perovskites: (left)  $\text{CsBr}$  termination for Type 1 and (right)  $\text{SnBr}_2$  termination for Type 2. The top left corner is a model of bulk  $\text{CsSnBr}_3$ .

### 3. Results and Discussion

In our simulation, the structures of  $\text{Cs}_{n+1}\text{Sn}_n\text{Br}_{3n+1}$  and  $\text{Cs}_n\text{Sn}_{n+1}\text{Br}_{3n+2}$  was optimized and all atoms were allowed to relax. The degree of surface rumpling was quantitatively described to reveal the difference between the two structures. A variable  $d_{i,i+1}$  can be defined as the interplanar distance between the neighboring atomic planes. The index  $i$  labels the atomic layers of Type 1 and Type 2 in Figure 1. The relative displacements are described using the following nondimensional quantity equation [32]:

$$\delta_{i,i+1} = \frac{d_{i,i+1} - a_0/2}{a_0}, \quad (1)$$

where  $a_0$  is the theoretical lattice constant calculated for bulk  $\text{CsSnBr}_3$ .

$\delta_{i,i+1}$  is related with the vacuum layer. For example, in  $\text{Cs}_3\text{Sn}_2\text{Br}_7$  ( $n = 2$ ) of Type 1, the relative displacements  $\delta_{1,2}$  and  $\delta_{2,3}$  were  $-1.05$  and  $1.69\%$ , respectively. All relative displacements,  $\delta_{i,i+1}$ , are shown in Table 1 for layers 1 to 5. The structures of  $\text{Cs}_{n+1}\text{Sn}_n\text{Br}_{3n+1}$  and  $\text{Cs}_n\text{Sn}_{n+1}\text{Br}_{3n+2}$  were centrosymmetric and  $\delta_{i,i+1}$  gradually decreased from the terminated surface to the symmetric center. This trend implies that the stability of the octahedral structure near the center of symmetry was better than that of the terminated surface. We also found that the relative displacements  $\delta_{1,2}$  for Type 1 were bigger than that for Type 2, which means  $\text{Cs}_{n+1}\text{Sn}_n\text{Br}_{3n+1}$  with  $\text{CsBr}$ -termination had better stability than  $\text{Cs}_n\text{Sn}_{n+1}\text{Br}_{3n+2}$ . Our conclusion is consistent with the previous calculation [32].

**Table 1.** Calculated relative displacements,  $\delta_{i,i+1}$  (%), in unit of the calculated bulk CsSnBr<sub>3</sub> lattice constant), and layers rumpling,  $\eta_i$  (%), for Cs<sub>n+1</sub>Sn<sub>n</sub>Br<sub>3n+1</sub> and Cs<sub>n</sub>Sn<sub>n+1</sub>Br<sub>3n+2</sub> ( $n = 1-5$ ).

Layer ( $n$ )		1	2	3	4	5	
$\delta_{i,i+1}$ (%)	Type 1	Br <sub>1</sub> Sn <sub>2</sub>	0.6	-1.05	-1.56	-1.64	-1.71
		Sn <sub>2</sub> Br <sub>3</sub>		1.69	2.28	2.62	2.6
		Br <sub>3</sub> Sn <sub>4</sub>			0.004	-0.49	-0.69
		Sn <sub>4</sub> Br <sub>5</sub>				0.62	0.79
		Br <sub>5</sub> Sn <sub>6</sub>					0.02
	Type 2	Sn <sub>1</sub> Br <sub>2</sub>	-1.98	-2.68	-2.87	-2.9	-3
		Br <sub>2</sub> Sn <sub>3</sub>		0.24	1.14	1.52	1.69
		Sn <sub>3</sub> Br <sub>4</sub>			-0.74	-1.01	-1.13
		Br <sub>4</sub> Sn <sub>5</sub>				0.055	0.33
		Sn <sub>5</sub> Br <sub>6</sub>					-0.25
$\eta_i$ (%)	Type 1	Cs <sub>1</sub> Br <sub>1</sub> Cs <sub>1</sub>	-6.44	-8.28	-8.89	-8.78	-8.89
		Br <sub>2</sub> Sn <sub>2</sub> Br <sub>2</sub>	0	-1.78	-1.94	-1.89	-1.94
		Cs <sub>3</sub> Br <sub>3</sub> Cs <sub>3</sub>		0	-2.44	-3.11	-3.44
		Br <sub>4</sub> Sn <sub>4</sub> Br <sub>4</sub>			0	-0.17	-0.33
		Cs <sub>5</sub> Br <sub>5</sub> Cs <sub>5</sub>				0	-0.72
	Type 2	Br <sub>6</sub> Sn <sub>6</sub> Br <sub>6</sub>					0
		Br <sub>1</sub> Sn <sub>1</sub> Br <sub>1</sub>	-3.22	-3.28	-3.17	-2.94	-2.83
		Cs <sub>2</sub> Br <sub>2</sub> Cs <sub>2</sub>	0	-2.11	-2.83	-3.28	-3.67
		Br <sub>3</sub> Sn <sub>3</sub> Br <sub>3</sub>		0	-0.078	-1	-1
		Cs <sub>4</sub> Br <sub>4</sub> Cs <sub>4</sub>			0	-0.89	-1.28
	Br <sub>5</sub> Sn <sub>5</sub> Br <sub>5</sub>				0	-0.22	
	Cs <sub>6</sub> Br <sub>6</sub> Cs <sub>6</sub>					0	

The ratio of angle change before and after optimization can be defined to correspond with the degree of surface rumpling with bond angles in the same atomic plane. The equation is as follows:

$$\eta_{i,i+1} = \frac{\theta_{i,i+1} - \pi}{\pi}, \quad (2)$$

where  $\theta$  is the degree of Cs<sub>i</sub>Br<sub>i</sub>Cs<sub>i</sub> or Br<sub>i</sub>Sn<sub>i</sub>Br<sub>i</sub> ( $i = 1-5$ ); namely, two Cs atoms are non-adjacent in the CsBr plane or two Br atoms are along the y direction in the SnBr<sub>2</sub> plane. Compared with the angles of CsBrCs, the angles of BrSnBr forming octahedral frames change slightly. When  $n = 4$  and  $5$ , the layers rumpling,  $\eta_i$ , of CsBrCs and BrSnBr decreased to zero from the terminated surface to the symmetric center. In Type 1, the structure of Cs<sub>n+1</sub>Sn<sub>n</sub>Br<sub>3n+1</sub> contained one or more complete perovskite structures (ABX<sub>3</sub>), in which the shape of the band structure had no change and only the value of the band energy varied with the layers from 1 to 5. It is noticed that Cs<sub>n</sub>Sn<sub>n+1</sub>Br<sub>3n+2</sub> contains SnBr<sub>2</sub> termination on the top and bottom surfaces in addition to one or more ABX<sub>3</sub> in the Type 1 model. Therefore, compared to the structures of Cs<sub>n+1</sub>Sn<sub>n</sub>Br<sub>3n+1</sub> and Cs<sub>n</sub>Sn<sub>n+1</sub>Br<sub>3n+2</sub>, we inferred that the change of band structure shape of Cs<sub>n</sub>Sn<sub>n+1</sub>Br<sub>3n+2</sub> was induced by the SnBr<sub>2</sub>-terminated surface.

Figure 2 shows the electron density difference of Cs<sub>n+1</sub>Sn<sub>n</sub>Br<sub>3n+1</sub> and Cs<sub>n</sub>Sn<sub>n+1</sub>Br<sub>3n+2</sub> in the slice plane (0.5, 0, 0) with different layer numbers. Obviously, the lost charge of the Sn atom transferred to the six adjacent Br atoms, and it is asymmetric along the z direction. The length of the Sn–Br bond is inversely proportional to the electron density; that is, the larger the electron density, the shorter the bond. This asymmetry gradually decreases along the z direction from the terminated surface to the symmetry center. This is consistent with the changes in  $\delta_{i,i+1}$ , which gradually decreased from the terminated surface to the center of symmetry.

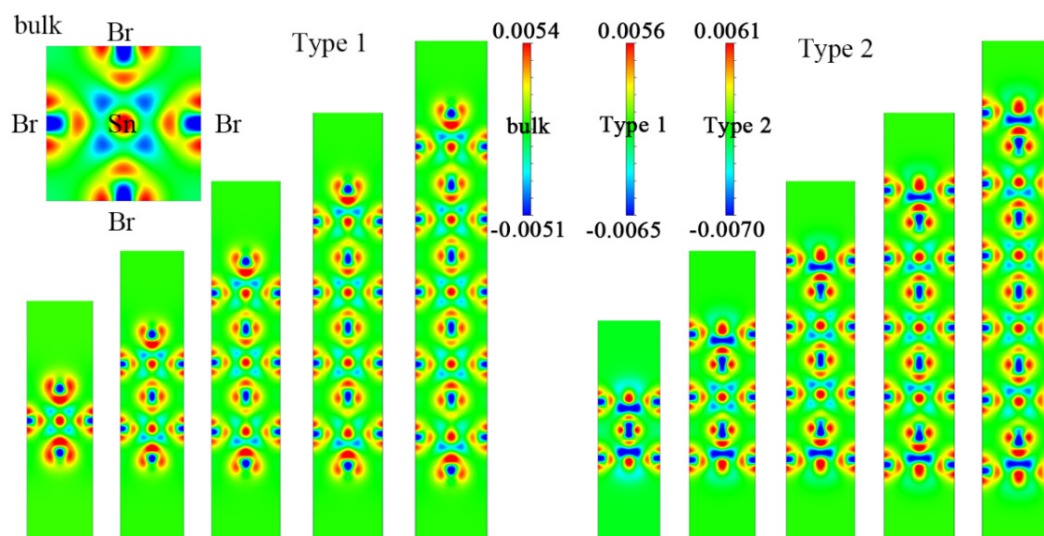


**Figure 2.** Electron density difference in the slice plane (0.5, 0, 0) in  $\text{Cs}_{n+1}\text{Sn}_n\text{Br}_{3n+1}$  and  $\text{Cs}_n\text{Sn}_{n+1}\text{Br}_{3n+2}$  ( $n = 1-5$ ). The top left corner is the electron density difference of the bulk  $\text{CsSnBr}_3$ . The scale is in electrons/Å.

The calculated bandgap energies of  $\text{Cs}_{n+1}\text{Sn}_n\text{Br}_{3n+1}$  and  $\text{Cs}_n\text{Sn}_{n+1}\text{Br}_{3n+2}$  ( $n = 1-5$ ) are listed in Table 2. As  $n$  increases from 1 to 5, the bandgap energies of  $\text{Cs}_{n+1}\text{Sn}_n\text{Br}_{3n+1}$  and  $\text{Cs}_n\text{Sn}_{n+1}\text{Br}_{3n+2}$  decrease from 1.209 to 0.797 eV and 1.310 to 1.013 eV, respectively. Our calculations are almost the same as those calculated by Anu et al. Their results showed that the bandgap energies of  $\text{Cs}_{n+1}\text{Sn}_n\text{Br}_{3n+1}$  are 1.2 eV, 1.04 eV, 0.92 eV, 0.85 eV and 0.79 eV with the layers from 1 to 5 [53]. In experiments, it was also found that the bandgap energies of  $(\text{PEA})_2(\text{MA})_{n-1}\text{Pb}_n\text{Br}_{3n+1}$  (2D) and  $(\text{CH}_3(\text{CH}_2)_3\text{NH}_3)_2(\text{CH}_3\text{NH}_3)_{n-1}\text{Pb}_n\text{I}_{3n+1}$  (2D) gradually shrink with the increase in the layer number [41,42]. There are many publications which support our models [31,32,54–56]. As shown in Figure 3a–e, the conduction band minimum (CBM) and the valence band maximum (VBM) of Type 1 appear at the R point (0.5, 0.5, 0.5). The bandgap of  $\text{Cs}_{n+1}\text{Sn}_n\text{Br}_{3n+1}$  presents a direct bandgap and gradually shrinks with the increase in the layer number. According to this trend, the bandgap of  $\text{Cs}_{n+1}\text{Sn}_n\text{Br}_{3n+1}$  will reach 0.641 eV with the increase of  $n$  [54]. The bandgap of  $\text{Cs}_n\text{Sn}_{n+1}\text{Br}_{3n+2}$  also decreases with the increase of  $n$ . However, unlike that of  $\text{Cs}_{n+1}\text{Sn}_n\text{Br}_{3n+1}$ , the band structure of  $\text{Cs}_n\text{Sn}_{n+1}\text{Br}_{3n+2}$  in Figure 4 shows an indirect bandgap because the CBM of  $\text{Cs}_n\text{Sn}_{n+1}\text{Br}_{3n+2}$  does not appear at the M point (0.5, 0.5, 0) when  $n = 1, 2$  and 3 (Figure 4a–c). It can be seen that the band structure at the bottom of the conduction band along the  $\text{M} \rightarrow \text{X}$  and  $\text{M} \rightarrow \Gamma$  directions is W-shaped ( $n = 1, 2$  and 3) instead of parabolic, as shown in Figure 4. When  $n = 1, 2$  and 3, the differences between the M point (0.5, 0.5, 0) and the lowest point are 26.6, 8.7 and 1.8 meV, respectively. With the increase of  $n$ , the differences gradually decrease to zero when  $n = 4$  and 5 (Figure 4d,e), which means the band structure of  $\text{Cs}_n\text{Sn}_{n+1}\text{Br}_{3n+2}$  turns into a direct bandgap. The band structures of  $\text{Cs}_n\text{Sn}_{n+1}\text{Br}_{3n+2}$  ( $n = 1$ ) calculated by PBE and HSE06 DFT are shown in Supplementary Figure S1. It is easy to see that the band structure of  $\text{Cs}_n\text{Sn}_{n+1}\text{Br}_{3n+2}$  ( $n = 1$ ) calculated by HSE06 has a shift up compared with that by the PBE calculation, while the shape of the band does not change. In view of the high computational cost, PBE is used in this work.

**Table 2.** Calculated bandgap energies (in eV) of  $\text{Cs}_{n+1}\text{Sn}_n\text{Br}_{3n+1}$  and  $\text{Cs}_n\text{Sn}_{n+1}\text{Br}_{3n+2}$  ( $n = 1-5$ ). The *d* and *ind* in parentheses represent direct and indirect bandgap, respectively.

Layer ( $n$ )	1	2	3	4	5	Bulk
Type 1	1.209 ( <i>d</i> )	1.036 ( <i>d</i> )	0.928 ( <i>d</i> )	0.851 ( <i>d</i> )	0.797 ( <i>d</i> )	
Type 2	1.310 ( <i>ind</i> )	1.266 ( <i>ind</i> )	1.198 ( <i>ind</i> )	1.100 ( <i>d</i> )	1.013 ( <i>d</i> )	0.641

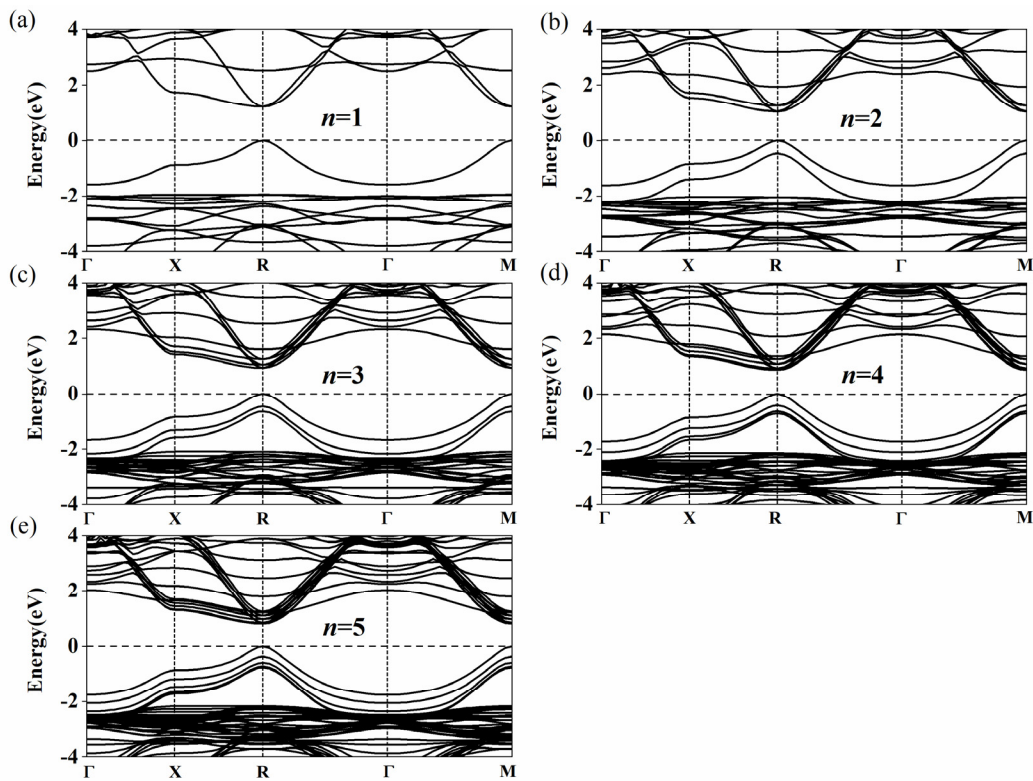


**Figure 3.** Calculated band structures of  $Cs_{n+1}Sn_nBr_{3n+1}$  for (a) 1 layer, (b) 2 layers, (c) 3 layers, (d) 4 layers and (e) 5 layers. The CBM and the VBM appear at the R point (0.5 0.5 0.5). The high symmetry path is assumed with respect to the Brillouin zone center  $\Gamma$  with the coordinates (0, 0, 0) to X (0, 0.5, 0), R (0.5, 0.5, 0.5),  $\Gamma$  (0, 0, 0) and M (0.5, 0.5, 0).

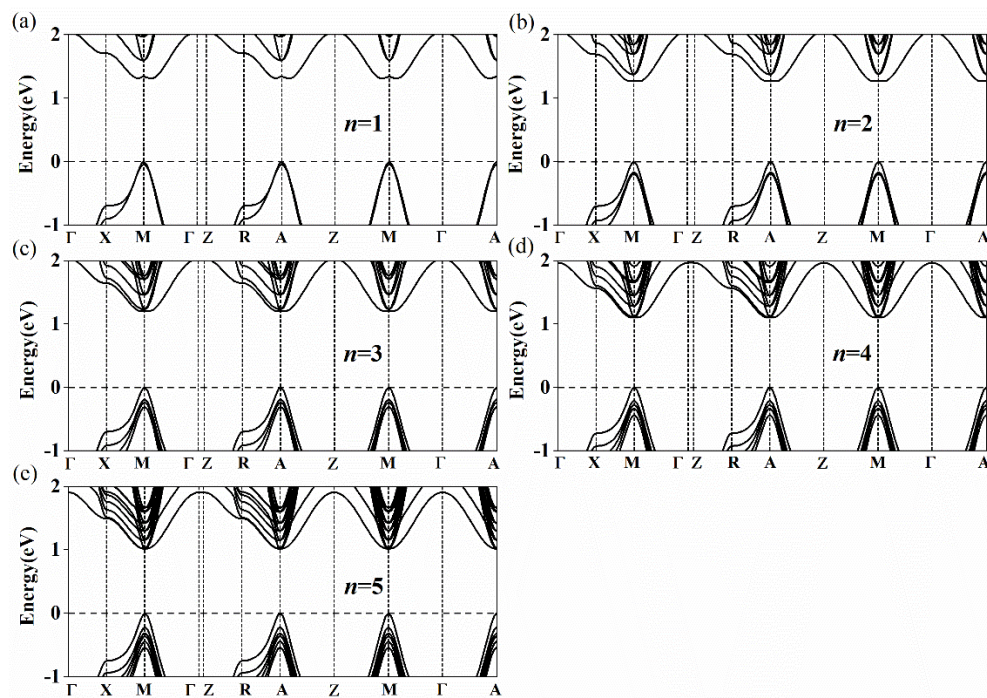


**Figure 4.** Calculated band structures of  $Cs_nSn_{n+1}Br_{3n+2}$  for (a) 1 layer, (b) 2 layers, (c) 3 layers, (d) 4 layers and (e) 5 layers. The high symmetry path is assumed with respect to the Brillouin zone center  $\Gamma$  with the coordinates (0, 0, 0) to X (0, 0.5, 0), M (0.5, 0.5, 0),  $\Gamma$  (0, 0, 0), Z (0, 0, 0.5), R (0, 0.5, 0.5), A (0.5, 0.5, 0.5), Z (0, 0, 0.5), M (0.5, 0.5, 0),  $\Gamma$  (0, 0, 0) and A (0.5, 0.5, 0.5).

To carefully examine which atom induces the emergence of the indirect bandgap of  $\text{Cs}_n\text{Sn}_{n+1}\text{Br}_{3n+2}$ , the density of states (DOS) of both types with  $n = 1$  and  $5$  were calculated, as shown in Figure 5. Figure 5 indicates that the Sn state plays a dominant role, while the Cs state is negligible for the valence band top and conduction band bottom in both models. It can be seen that a small peak appears at the bottom of the conduction band of  $\text{Cs}_{n+1}\text{Sn}_n\text{Br}_{3n+1}$  (Type 1,  $n = 1$ ; indicated by an arrow), which is induced by the degeneracy of energy levels (Figure 5a). Figure 5b shows that the valence band top and conduction band bottom of  $\text{Cs}_n\text{Sn}_{n+1}\text{Br}_{3n+2}$  (Type 2) are dominated by Br and Sn states. A sharp and strong peak (indicated by an arrow) appears for the DOS of  $\text{Cs}_n\text{Sn}_{n+1}\text{Br}_{3n+2}$  ( $n = 1$ ), which indicates that the generation of an indirect bandgap is induced by Sn atoms. The intensity of the peak (indicated by an arrow) of  $\text{Cs}_n\text{Sn}_{n+1}\text{Br}_{3n+2}$  decreases gradually with layer numbers from 1 to 5, which means a transition from indirect to direct bandgap for  $\text{Cs}_n\text{Sn}_{n+1}\text{Br}_{3n+2}$ . Therefore, according to the DOS in Figure 5,  $\text{Cs}_{n+1}\text{Sn}_n\text{Br}_{3n+1}$  is a direct bandgap and  $\text{Cs}_n\text{Sn}_{n+1}\text{Br}_{3n+2}$  is an indirect bandgap led by Sn atoms.

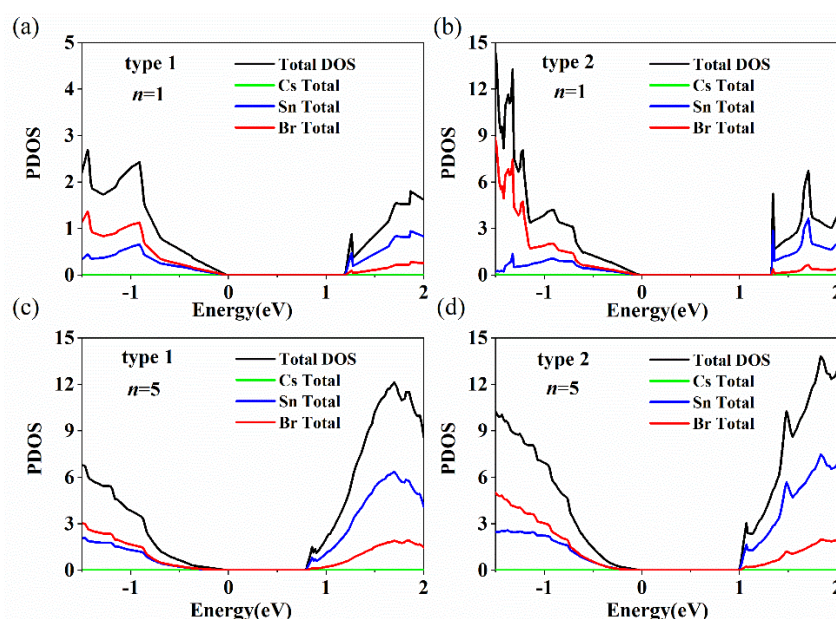


**Figure 5.** Calculated DOS for  $\text{Cs}_{n+1}\text{Sn}_n\text{Br}_{3n+1}$  and  $\text{Cs}_n\text{Sn}_{n+1}\text{Br}_{3n+2}$  with  $n = 1$  and  $5$ . The arrow points to the peaks of Type 1 and Type 2 at  $n = 1$ . The green, blue, red, and black lines represent Cs TDOS, Sn TDOS, Br TDOS and TDOS, respectively. The models are (a)  $\text{Cs}_{n+1}\text{Sn}_n\text{Br}_{3n+1}$  ( $n = 1$ ), (b)  $\text{Cs}_n\text{Sn}_{n+1}\text{Br}_{3n+2}$  ( $n = 1$ ), (c)  $\text{Cs}_{n+1}\text{Sn}_n\text{Br}_{3n+1}$  ( $n = 5$ ) and (d)  $\text{Cs}_n\text{Sn}_{n+1}\text{Br}_{3n+2}$  ( $n = 5$ ).

Further efforts were made to separately calculate the partial density of states (PDOS) of Sn and Br atoms at the terminated surface in Figure 6 (the two atoms are indicated by arrows in Supplementary Figure S2). The results show that the conduction band bottom of  $\text{Cs}_n\text{Sn}_{n+1}\text{Br}_{3n+2}$  is mainly dominated by the  $5p$ -Sn state. The peak of total DOS of Sn atoms in Figure 5b is 2.87, and the peak of PDOS of the Sn atom in Figure 6a is 1.41; there is about a twofold relationship between the size of the peak. It is also found that the contribution of the  $4p$ -Br state to the conduction band bottom of  $\text{Cs}_n\text{Sn}_{n+1}\text{Br}_{3n+2}$  is negligible according to Figure 6b. Therefore, the  $5p$ -Sn state at the terminated surface induced the generation of an indirect bandgap for  $\text{Cs}_n\text{Sn}_{n+1}\text{Br}_{3n+2}$ . In addition, we calculated the orbital-projected band structures of  $\text{Cs}_n\text{Sn}_{n+1}\text{Br}_{3n+2}$  ( $n = 1$ ) in Supplementary Figure S2a, which coincides completely with the calculated band structures in Figure 4a. This alignment indicates that the conduction band bottom of  $\text{Cs}_n\text{Sn}_{n+1}\text{Br}_{3n+2}$  is dominated by the  $5p$ -Sn state, which agrees well with the PDOS calculations for Sn and Br atoms.

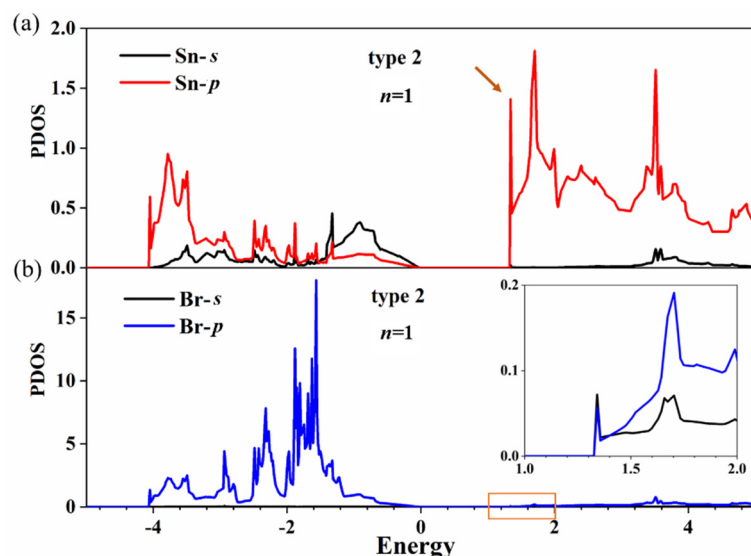


**Figure 6.** PDOS of Sn (a) and Br (b) atoms in the SnBr<sub>2</sub>-terminated surface for Cs<sub>n</sub>Sn<sub>n+1</sub>Br<sub>3n+2</sub> ( $n = 1$ ). The inset of (b) is an enlargement of the orange box.

A suitable bandgap energy and large absorption coefficient are important for photoelectric and photovoltaic devices. Therefore, the optical absorption of Cs<sub>n+1</sub>Sn<sub>n</sub>Br<sub>3n+1</sub> and Cs<sub>n</sub>Sn<sub>n+1</sub>Br<sub>3n+2</sub>, with different layer numbers, have also been studied in this work. The optical absorption is generally calculated using the complex dielectric function, which is expressed as  $\epsilon(\omega) = \epsilon_1(\omega) + i\epsilon_2(\omega)$ , where  $\omega$  is the frequency of light,  $\epsilon_1$  and  $\epsilon_2$  are the real and imaginary parts of the dielectric function, respectively.  $\epsilon_2$  is usually used to describe the light absorption behavior and its specific description is given by the following equation [57]:

$$\epsilon_2(\omega) = \frac{Ve^2}{2\pi\hbar m^2 \omega^2} \int d^3k \sum_{nn'} |\langle kn|p|kn' \rangle|^2 f(kn) * (1 - f(kn')) \delta(E_{kn} - E_{kn'} - \hbar\omega), \quad (3)$$

where  $V$  is unit volume,  $e$  represents electron charge,  $m$  is the electron rest mass,  $p$  is the momentum transition matrix,  $\hbar$  is the reduced Planck Constant;  $kn$  and  $kn'$  are the wave functions of the conduction band and valence band, respectively. In order to rapidly distinguish these physical variables, we show them in the Supplementary Table S1. Moreover, by using the Kramers–Kronig relationship, the real part of the dielectric function is obtained as follows [58]:

$$\epsilon_1(\omega) = 1 + \frac{2}{\pi} P \int_0^\infty \frac{\epsilon_2(\omega') \omega' d\omega'}{\omega'^2 - \omega^2}, \quad (4)$$

where  $P$  is the principal value of the integral. The absorption coefficient is given as follows [59]:

$$\alpha = 2\omega \left[ \frac{(\epsilon_1^2(\omega) + \epsilon_2^2(\omega))^{1/2} - \epsilon_1(\omega)}{2} \right]^{1/2}, \quad (5)$$

The absorption coefficient is a key parameter and is of great significance in photoelectric and photovoltaic applications. Figure 7 shows the absorption spectra of Cs<sub>n+1</sub>Sn<sub>n</sub>Br<sub>3n+1</sub> and Cs<sub>n</sub>Sn<sub>n+1</sub>Br<sub>3n+2</sub> with different layer numbers along the  $x$ ,  $y$  (Figure 7a,c) and  $z$  (Figure 7b,d) directions. Both Cs<sub>n+1</sub>Sn<sub>n</sub>Br<sub>3n+1</sub> and Cs<sub>n</sub>Sn<sub>n+1</sub>Br<sub>3n+2</sub> have large light absorption coefficients in the visible and infrared regions. With the decrease in layer number, the absorption coefficients of both Cs<sub>n+1</sub>Sn<sub>n</sub>Br<sub>3n+1</sub> and Cs<sub>n</sub>Sn<sub>n+1</sub>Br<sub>3n+2</sub> have redshift. Different from that of bulk CsSnBr<sub>3</sub>, the light absorption of Cs<sub>n+1</sub>Sn<sub>n</sub>Br<sub>3n+1</sub> and Cs<sub>n</sub>Sn<sub>n+1</sub>Br<sub>3n+2</sub> show anisotropy. In the visible region, the absorption coefficients for Cs<sub>n</sub>Sn<sub>n+1</sub>Br<sub>3n+2</sub> along the  $x$  and  $y$  directions are very close to and smaller than those for bulk CsSnBr<sub>3</sub> (Figure 7c); the layer dependence is not strong. This behavior is related to the absorption of Sn and Br



atoms in the terminated surface.  $\text{Cs}_n\text{Sn}_{n+1}\text{Br}_{3n+2}$  has a larger absorption coefficient than  $\text{Cs}_{n+1}\text{Sn}_n\text{Br}_{3n+1}$  along the  $x$  and  $y$  directions (Figure 7a,c). The SnBr-terminated surface model provides an ideal model for the design of 2D RP perovskites for photovoltaic and optoelectronic devices.

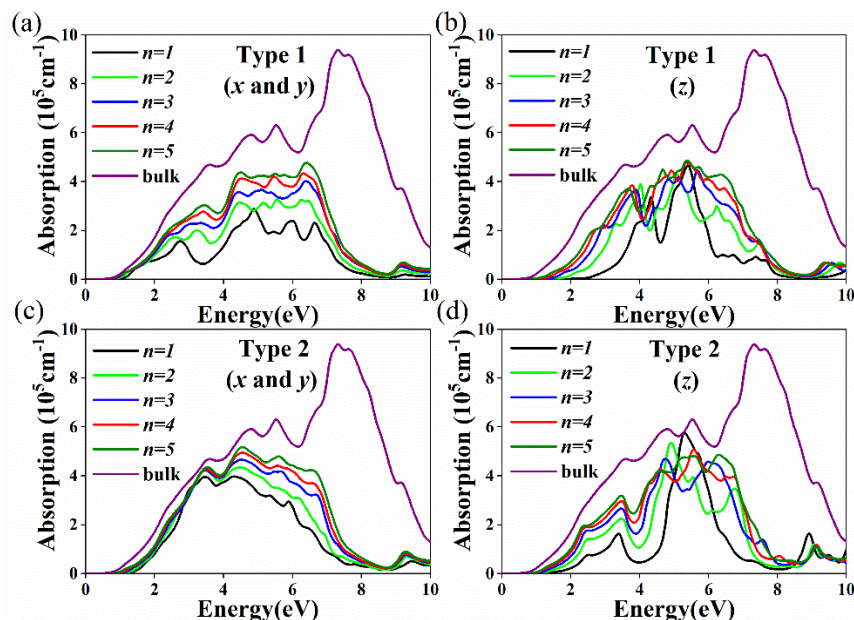


**Figure 7.** Calculated absorption coefficient for (a)  $\text{Cs}_{n+1}\text{Sn}_n\text{Br}_{3n+1}$  ( $n = 1-5$ )  $x$  and  $y$  directions; (b)  $\text{Cs}_{n+1}\text{Sn}_n\text{Br}_{3n+1}$  ( $n = 1-5$ )  $z$  directions; and (c)  $\text{Cs}_n\text{Sn}_{n+1}\text{Br}_{3n+2}$  ( $n = 1-5$ )  $x$  and  $y$  directions; (d)  $\text{Cs}_n\text{Sn}_{n+1}\text{Br}_{3n+2}$  ( $n = 1-5$ )  $z$  directions.

#### 4. Conclusions

In conclusion, based on the cubic  $\text{CsSnBr}_3$ , we designed two models in this work, including  $\text{Cs}_{n+1}\text{Sn}_n\text{Br}_{3n+1}$  with CsBr-termination and  $\text{Cs}_n\text{Sn}_{n+1}\text{Br}_{3n+2}$  with SnBr<sub>2</sub>-termination. Their bandgap energies, structural and optoelectronic properties of the two models were calculated using DFT. The calculated results indicated that the band structure of  $\text{Cs}_{n+1}\text{Sn}_n\text{Br}_{3n+1}$  is a direct bandgap. Additionally, the band structure of  $\text{Cs}_n\text{Sn}_{n+1}\text{Br}_{3n+2}$  can be altered from an indirect to direct bandgap with the increase in the layer numbers. With the variation of the layer number from 1 to 5, the bandgaps of  $\text{Cs}_{n+1}\text{Sn}_n\text{Br}_{3n+1}$  and  $\text{Cs}_n\text{Sn}_{n+1}\text{Br}_{3n+2}$  decreased from 1.209 to 0.797 eV and 1.310 to 1.013 eV, respectively. Furthermore, we calculated the DOS of Sn and Br atoms and the orbital-projected band structures of  $\text{Cs}_n\text{Sn}_{n+1}\text{Br}_{3n+2}$  ( $n = 1$ ) in the terminated surface. It was found that the  $5p$ -Sn state was responsible for the appearance of the indirect bandgap of  $\text{Cs}_n\text{Sn}_{n+1}\text{Br}_{3n+2}$ . In addition, both  $\text{Cs}_{n+1}\text{Sn}_n\text{Br}_{3n+1}$  and  $\text{Cs}_n\text{Sn}_{n+1}\text{Br}_{3n+2}$  have as large of an absorption coefficient as bulk  $\text{CsSnBr}_3$  and show anisotropy. Nevertheless,  $\text{Cs}_n\text{Sn}_{n+1}\text{Br}_{3n+2}$  exhibits an insensitivity to the layer number along the  $x$  and  $y$  directions. The calculated results obtained in this work may provide new ideas for the design of photovoltaic devices.

**Supplementary Materials:** The following are available online at <https://www.mdpi.com/article/10.3390/nano11082119/s1>, Figure S1: band structure of  $\text{Cs}_n\text{Sn}_{n+1}\text{Br}_{3n+2}$  ( $n = 1$ ) calculated by PBE (black lines) and HSE06 (red lines) DFT; Figure S2: (a) Orbital-projected band structures of  $\text{Cs}_n\text{Sn}_{n+1}\text{Br}_{3n+2}$  ( $n = 1$ ). (b) Model of  $\text{Cs}_n\text{Sn}_{n+1}\text{Br}_{3n+2}$  ( $n = 1$ ); Table S1. the variables used in this work, including variables' names and physical meanings.

**Author Contributions:** Conceptualization, G.X.; J.L. and H.M.; theoretical calculation, G.X.; Y.W. and C.C.; writing—original draft preparation, G.X., Y.L.; C.C. and H.M.; writing—review and editing, H.M. and J.L.; supervision, funding acquisition, J.L., C.C. and H.M. All authors have read and agreed to the published version of the manuscript.

**Funding:** This work was funded by the project ZR2020MA081, ZR2019MA037 and ZR2018BA031 supported by Shandong Provincial Nature Science Foundation. This work also received the financial support from by the National Natural Science Foundation of China (NFSC) (grant No. 11904212) and the Research Leader Program of Jinan Science and Technology Bureau (2019GXRC061).

**Data Availability Statement:** Data are contained within the article.

**Conflicts of Interest:** The authors declare no conflict of interest.

## References

1. Liu, X.K.; Xu, W.; Bai, S.; Jin, Y.; Wang, J.; Friend, R.H.; Gao, F. Metal halide perovskites for light-emitting diodes. *Nat. Mater.* **2021**, *20*, 10–21. [[CrossRef](#)] [[PubMed](#)]
2. Jia, Y.; Kerner, R.A.; Grede, A.J.; Rand, B.P.; Giebink, N.C. Continuous-wave lasing in an organic-inorganic lead halide semiconductor. *Nat. Photonics* **2017**, *11*, 784–788. [[CrossRef](#)]
3. Fu, Y.; Zhu, H.; Stoumpos, C.C.; Ding, Q.; Wang, J.; Kanatzidis, M.G.; Zhu, X.; Jin, S. Broad Wavelength Tunable Robust Lasing from Single-Crystal Nanowires of Cesium Lead Halide Perovskites (CsPbX<sub>3</sub>, X = Cl, Br, I). *ACS Nano* **2016**, *10*, 7963–7972. [[CrossRef](#)] [[PubMed](#)]
4. Kim, J.Y.; Lee, J.W.; Jung, H.S.; Shin, H.; Park, N.G. High-Efficiency Perovskite Solar Cells. *Chem* **2020**, *120*, 7867–7918.
5. Lin, K.; Xing, J.; Quan, L.; Arquer, F.P.G.; Gong, X.; Lu, J.; Xie, L.; Zhao, W.; Zhang, D.; Yan, C.; et al. Perovskite light-emitting diodes with external quantum efficiency exceeding 20 per cent. *Nature* **2018**, *562*, 245–248. [[CrossRef](#)]
6. Chen, B.; Yu, Z.; Liu, K.; Zheng, X.; Liu, Y.; Shi, J.; Spronk, D.; Rudd, P.N.; Holman, Z.; Huang, J. Grain Engineering for Perovskite/Silicon Monolithic Tandem Solar Cells with Efficiency of 25.4%. *Joule* **2019**, *3*, 177–190. [[CrossRef](#)]
7. Turren-Cruz, S.H.; Saliba, M.; Mayer, M.T.; Juárez-Santiesteban, H.; Mathew, X.; Nienhaus, L.; Tress, W.; Erodici, M.P.; Sher, M.J.; Bawendi, M.G.; et al. Enhanced charge carrier mobility and lifetime suppress hysteresis and improve efficiency in planar perovskite solar cells. *Energy Environ. Sci.* **2018**, *11*, 78–86. [[CrossRef](#)]
8. Chen, B.; Baek, S.W.; Hou, Y.; Aydin, E.; Bastiani, M.D.; Scheffel, B.; Proppe, A.; Huang, Z.; Wei, M.; Wang, Y.; et al. Enhanced optical path and electron diffusion length enable high-efficiency perovskite tandems. *Nat. Commun.* **2020**, *11*, 1257. [[CrossRef](#)]
9. Qiu, X.; Cao, B.; Yuan, S.; Chen, X.; Qiu, Z.; Jiang, Y.; Ye, Q.; Wang, H.; Zeng, H.; Liu, J.; et al. From unstable CsSnI<sub>3</sub> to air-stable Cs<sub>2</sub>SnI<sub>6</sub>: A lead-free perovskite solar cell light absorber with bandgap of 1.48 eV and high absorption coefficient. *Sol. Energy Mater. Sol. Cells* **2017**, *159*, 227–234. [[CrossRef](#)]
10. Giorgi, G.; Fujisawa, J.I.; Segawa, H.; Yamashita, K. Small Photocarrier Effective Masses Featuring Ambipolar Transport in Methylammonium Lead Iodide Perovskite: A Density Functional Analysis. *J. Phys. Chem. Lett.* **2013**, *4*, 4213–4216. [[CrossRef](#)]
11. Leng, K.; Abdelwahab, I.; Verzhbitskiy, I.; Telychko, M.; Chu, L.; Fu, W.; Chi, X.; Guo, N.; Chen, Z.; Chen, Z.; et al. Molecularly thin two-dimensional hybrid perovskites with tunable optoelectronic properties due to reversible surface relaxation. *Nat. Mater.* **2018**, *17*, 908–914. [[CrossRef](#)]
12. Shao, H.; Bai, X.; Cui, H.; Pan, G.; Jing, P.; Qu, S.; Zhu, J.; Zhai, Y.; Dong, B.; Song, H. White light emission in Bi<sup>3+</sup>/Mn<sup>2+</sup> ion co-doped CsPbCl<sub>3</sub> perovskite nanocrystals. *Nanoscale* **2018**, *10*, 1023–1029. [[CrossRef](#)]
13. Braly, I.L.; Quillettes, D.W.; Pazos-Outón, L.M.; Burke, S.; Ziffer, M.E.; Ginger, D.S.; Hillhouse, H.W. Hybrid perovskite films approaching the radiative limit with over 90% photoluminescence quantum efficiency. *Nat. Photonics* **2018**, *12*, 355–361. [[CrossRef](#)]
14. Yang, S.; Chen, S.; Mosconi, E.; Fang, Y.; Xiao, X.; Wang, C.; Zhou, Y.; Yu, Z.; Zhao, J.; Gao, Y.; et al. Stabilizing halide perovskite surfaces for solar cell operation with wide-bandgap lead oxysalts. *Science* **2019**, *365*, 473–478. [[CrossRef](#)] [[PubMed](#)]
15. Zhou, L.; Guo, X.; Lin, Z.; Ma, J.; Su, J.; Hu, Z.; Zhang, C.; Liu, S.; Chang, J.; Hao, Y. Interface engineering of low temperature processed all-inorganic CsPbI<sub>2</sub>Br perovskite solar cells toward PCE exceeding 14%. *Nano Energy* **2019**, *60*, 583–590. [[CrossRef](#)]
16. Nishimura, K.; Kamarudin, M.A.; Hirotsu, D.; Hamada, K.; Shen, Q.; Iikubo, S.; Minemoto, T.; Yoshino, K.; Hayase, S. Lead-free tin-halide perovskite solar cells with 13% efficiency. *Nano Energy* **2020**, *74*, 104858. [[CrossRef](#)]
17. Kulbak, M.; Gupta, S.; Kedem, N.; Levine, I.; Bendikov, T.; Hodes, G.; Cahen, D. Cesium Enhances Long-Term Stability of Lead Bromide Perovskite-Based Solar Cells. *J. Phys. Chem. Lett.* **2016**, *7*, 167–172. [[CrossRef](#)]
18. Ren, H.; Yu, S.; Chao, L.; Xia, Y.; Sun, Y.; Zuo, S.; Li, F.; Niu, T.; Yang, Y.; Ju, H.; et al. Efficient and stable Ruddlesden-Popper perovskite solar cell with tailored interlayer molecular interaction. *Nat. Photonics* **2020**, *14*, 154–163. [[CrossRef](#)]
19. Lai, H.; Kan, B.; Liu, T.; Zheng, N.; Xie, Z.; Zhou, T.; Wan, X.; Zhang, X.; Liu, Y.; Chen, Y. Two-dimensional Ruddlesden-Popper perovskite with nanorod-like morphology for solar cells with efficiency exceeding 15%. *J. Am. Chem. Soc.* **2018**, *140*, 11639–11646. [[CrossRef](#)]
20. Li, M.H.; Yeh, H.H.; Chiang, Y.H.; Jeng, U.S.; Su, C.J.; Shiu, H.W.; Hsu, Y.J.; Kosugi, N.; Ohigashi, T.; Chen, Y.A.; et al. Highly Efficient 2D/3D Hybrid Perovskite Solar Cells via Low-Pressure Vapor-Assisted Solution Process. *Adv. Mater.* **2018**, *30*, 1801401. [[CrossRef](#)]
21. Liu, B.; Long, M.; Cai, M.; Ding, L.; Yang, J. Interfacial charge behavior modulation in 2D/3D perovskite heterostructure for potential high-performance solar cells. *Nano Energy* **2019**, *59*, 715–720. [[CrossRef](#)]
22. Lee, H.D.; Kim, H.; Cho, H.; Cha, W.; Hong, Y.; Kim, Y.H.; Sadhanala, A.; Venugopalan, V.; Kim, J.S.; Choi, J.W.; et al. Efficient Ruddlesden-Popper Perovskite Light-Emitting Diodes with Randomly Oriented Nanocrystals. *Adv. Funct. Mater.* **2019**, *29*, 1901225. [[CrossRef](#)]

23. Chinnambedu, R.M.; Chen, T.P.; Li, S.S.; Chen, W.L.; Lo, C.Y.; Liao, Y.M.; Haider, G.; Lin, C.C.; Chen, C.C.; Sankar, R.; et al. Low-Threshold Lasing from 2D Homologous Organic-Inorganic Hybrid Ruddlesden–Popper Perovskite Single Crystals. *Nano Lett.* **2018**, *18*, 3221–3228.
24. Wang, Z.; Lin, Q.; Chmiel, F.P.; Sakai, N.; Herz, L.M.; Snaith, H.J. Efficient ambient-air-stable solar cells with 2D-3D heterostructured butylammonium-caesium-formamidinium lead halide perovskites. *Nat. Energy* **2017**, *2*, 17135. [[CrossRef](#)]
25. Katan, C.; Mercier, N.; Even, J. Quantum and Dielectric Confinement Effects in Lower-Dimensional Hybrid Perovskite Semiconductors. *Chem. Asian J.* **2019**, *119*, 3140–3192. [[CrossRef](#)] [[PubMed](#)]
26. Tsai, H.; Nie, W.; Blancon, J.C.; Stoumpos, C.C.; Asadpour, R.; Harutyunyan, B.; Neukirch, A.J.; Verduzco, R.; Crochet, J.J.; Tretiak, S.; et al. High-efficiency two-dimensional Ruddlesden–Popper perovskite solar cells. *Nature* **2016**, *536*, 312–316. [[CrossRef](#)]
27. Zhang, F.; Lu, H.; Tong, J.; Berry, J.J.; Beard, M.C.; Zhu, K. Advances in two-dimensional organic-inorganic hybrid perovskites. *Energy Environ. Sci.* **2020**, *13*, 1154–1186. [[CrossRef](#)]
28. Qin, C.; Sandanayaka, A.S.D.; Zhao, C.; Matsushima, T.; Zhang, D.; Fujihara, T.; Adachi, C. Stable room-temperature continuous-wave lasing in quasi-2D perovskite films. *Nature* **2020**, *585*, 53–57. [[CrossRef](#)] [[PubMed](#)]
29. Mao, L.; Stoumpos, C.C.; Kanatzidis, M.G. Two-Dimensional Hybrid Halide Perovskites: Principles and Promises. *J. Am. Chem. Soc.* **2019**, *141*, 1171–1190. [[CrossRef](#)]
30. Vashishtha, P.; Ng, M.; Shivarudraiah, S.B.; Halpert, J.E. High Efficiency Blue and Green Light-Emitting Diodes Using Ruddlesden–Popper Inorganic Mixed alide Perovskites with Butylammonium Interlayers. *Chem. Mater.* **2018**, *31*, 83–89. [[CrossRef](#)]
31. Zhou, C.; Lin, H.; He, Q.; Xu, L.; Worku, M.; Chaaban, M.; Lee, S.; Shi, X.; Du, M.; Ma, B. Low dimensional metal halide perovskites and hybrids. *Mater. Sci. Eng. R Rep.* **2019**, *137*, 38–65. [[CrossRef](#)]
32. Pramchu, S.; Laosiritaworn, Y.; Jaroenjittichai, A.P. Electronic properties of surface/bulk iodine defects of CsSnBr<sub>3</sub> perovskite. *Surf. Coat. Technol.* **2016**, *306*, 159–163. [[CrossRef](#)]
33. Brik, M.G.; Ma, C.G.; Krasnenko, V. First-principles calculations of the structural and electronic properties of the cubic CaZrO<sub>3</sub> (001) surfaces. *Surf. Sci.* **2013**, *608*, 146–153. [[CrossRef](#)]
34. Liu, Q.; Liu, Z.; Chen, J.; Feng, L.; Tian, H.; Zeng, W. Structural and electronic properties of cubic SrHfO<sub>3</sub> surface: First principles calculations. *Appl. Surf. Sci.* **2012**, *258*, 3455–3461. [[CrossRef](#)]
35. Borstel, G.; Eglitis, R.I.; Kotomin, E.A.; Heifets, E. Modelling of defects and surfaces in perovskite ferroelectrics. *Phys. Stat. Sol.* **2003**, *236*, 253–264. [[CrossRef](#)]
36. Cheng, C.; Kunc, K.; Lee, M.H. Structural relaxation and longitudinal dipole moment of SrTiO<sub>3</sub> (001) (1 × 1) surfaces. *Phys. Rev. B* **2000**, *62*, 10409–10418. [[CrossRef](#)]
37. Eglitis, R.I. Ab initio calculations of SrTiO<sub>3</sub>, BaTiO<sub>3</sub>, PbTiO<sub>3</sub>, CaTiO<sub>3</sub>, SrZrO<sub>3</sub>, PbZrO<sub>3</sub> and BaZrO<sub>3</sub> (001), (011) and (111) surfaces as well as F centers, polarons, KTN solid solutions and Nb impurities therein. *Int. J. Mod. Phys. B* **2014**, *28*, 1430009. [[CrossRef](#)]
38. Padilla, J.; Vanderbilt, D. Ab initio study of SrTiO<sub>3</sub> surfaces. *Surf. Sci.* **1998**, *418*, 64–70. [[CrossRef](#)]
39. Heifets, E.; Eglitis, R.I.; Kotomin, E.A.; Maier, J.; Borstel, G. Ab initio modeling of surface structure for SrTiO<sub>3</sub> perovskite crystals. *Phys. Rev. B* **2001**, *64*, 235417. [[CrossRef](#)]
40. Wang, Y.; Arai, M.; Sasaki, T.; Wang, C.; Zhong, W. First-principles study on the (001) surface of cubic PbZrO<sub>3</sub> and PbTiO<sub>3</sub>. *Surf. Sci.* **2005**, *585*, 75–84. [[CrossRef](#)]
41. Cohen, B.E.; Wierzbowska, M.; Etgar, L. High Efficiency and High Open Circuit Voltage in Quasi 2D Perovskite Based Solar Cells. *Adv. Funct. Mater.* **2017**, *27*, 1604733. [[CrossRef](#)]
42. Cao, D.H.; Stoumpos, C.C.; Farha, O.K.; Hupp, J.T.; Kanatzidis, M.G. 2D Homologous Perovskites as Light-Absorbing Materials for Solar Cell Applications. *J. Am. Chem. Soc.* **2015**, *137*, 7843–7850. [[CrossRef](#)] [[PubMed](#)]
43. Charlton, G.; Brennan, S.; Muryn, C.A.; McGrath, R.; Norman, D.; Turner, T.S.; Thornton, G. Surface relaxation of SrTiO<sub>3</sub> (001). *Surf. Sci.* **2000**, *457*, L376–L380. [[CrossRef](#)]
44. Noguera, C. Polar oxide surfaces. *J. Phys. Condens. Matter* **2000**, *12*, R367–R410. [[CrossRef](#)]
45. Ikeda, A.; Nishimura, T.; Morishita, T.; Kido, Y. Surface relaxation and rumpling of TiO<sub>2</sub>-terminated SrTiO<sub>3</sub> (001) determined by medium energy ion scattering. *Surf. Sci.* **1999**, *433–435*, 520–524. [[CrossRef](#)]
46. Bickel, N.; Schmidt, G.; Heinz, K.; Müller, K. Ferroelectric Relaxation of the SrTiO<sub>3</sub> (100) Surface. *Phys. Rev. Lett.* **1989**, *62*, 2009–2011. [[CrossRef](#)] [[PubMed](#)]
47. Ma, C.G.; Krasnenko, V.; Brik, M.G. First-principles calculations of different (001) surface terminations of three cubic perovskites CsCaBr<sub>3</sub>, CsGeBr<sub>3</sub>, and CsSnBr<sub>3</sub>. *J. Phys. Chem. Solid* **2018**, *115*, 289–299. [[CrossRef](#)]
48. Runge, E.; Gross, E.K.U. Density-Functional Theory for Time-Dependent Systems. *Phys. Rev. Lett.* **1984**, *52*, 997–1000. [[CrossRef](#)]
49. Blochl, P.E. Projector augmented-wave method. *Phys. Rev. B* **1994**, *50*, 17953–17979. [[CrossRef](#)]
50. Perdew, J.P.; Burke, K.; Ernzerhof, M. Generalized gradient approximation made simple. *Phys. Rev. Lett.* **1996**, *77*, 3865. [[CrossRef](#)]
51. Kresse, G.; Furthmüller, J. Efficient iterative schemes for ab initio total-energy calculations using a plane-wave basis set. *Phys. Rev. B* **1996**, *54*, 11169. [[CrossRef](#)] [[PubMed](#)]
52. Monkhorst, H.J.; Pack, J.D. Special points for Brillouin-zone integrations. *Phys. Rev. B* **1976**, *13*, 5188–5192. [[CrossRef](#)]
53. Bala, A.; Deb, A.K.; Kumar, V. Atomic and Electronic Structure of Two-Dimensional Inorganic Halide Perovskites A<sub>n+1</sub>M<sub>n</sub>X<sub>3n+1</sub> (n = 1–6, A = Cs, M = Pb and Sn, and X = Cl, Br, and I) from ab Initio Calculations. *J. Phys. Chem. C* **2018**, *122*, 7464–7473. [[CrossRef](#)]

- 
54. Coduri, M.; Strobel, T.A.; Szafranski, M.; Katrusiak, A.; Mahata, A.; Cova, F.; Bonomi, S.; Mosconi, E.; Angelis, F.D.; Malavasi, L. Band Gap Engineering in  $\text{MASnBr}_3$  and  $\text{CsSnBr}_3$  Perovskites: Mechanistic Insights through the Application of Pressure. *J. Phys. Chem. Lett.* **2019**, *10*, 7398–7405. [[CrossRef](#)]
  55. Grote, C.; Ehrlich, B.; Berger, R.F. Tuning the near-gap electronic structure of tin-halide and lead-halide perovskites via changes in atomic layering. *Phys. Rev. B* **2014**, *90*, 205202. [[CrossRef](#)]
  56. Liu, B.; Long, M.; Cai, M.; Yang, J. Influence of the number of layers on ultrathin  $\text{CsSnI}_3$  perovskite: From electronic structure to carrier mobility. *J. Phys. D Appl. Phys.* **2018**, *51*, 105101. [[CrossRef](#)]
  57. Gao, L.; Tang, Y.; Diao, X. First-Principles Study on the Photoelectric Properties of  $\text{CsGeI}_3$  under Hydrostatic Pressure. *Appl. Sci.* **2020**, *10*, 5055. [[CrossRef](#)]
  58. Zhao, Y.; Liu, B.; Yu, Z.; Ma, J.; Wan, Q.; He, P.; Cai, M. Strong ferroelectric polarization of  $\text{CH}_3\text{NH}_3\text{GeI}_3$  with high-absorption and mobility transport anisotropy: Theoretical study. *J. Mater. Chem. C* **2017**, *5*, 5356–5364. [[CrossRef](#)]
  59. Yu, Z.; Ma, Q.; Liu, B.; Zhao, Y.; Wang, L.; Zhou, H.; Cai, M. Oriented tuning the photovoltaic properties of  $\gamma\text{-RbGeX}_3$  by strain-induced electron effective mass mutation. *J. Phys. D Appl. Phys.* **2017**, *50*, 465101. [[CrossRef](#)]